# Convection in rotating spherical fluid shells with inhomogeneous heat-flux at the outer boundary

By S. J. GIBBONS[1] †, D. GUBBINS[2] AND K. ZHANG[1]

[1]School of Mathematical Sciences,

University of Exeter, Exeter EX4 4QE

[2]School of Earth Sciences,

University of Leeds, Leeds LS2 9JT, UK

(Received 26 January 2001)

Previous work has studied the ability of lateral surface temperature variations to lock, or otherwise control, fluid flow in rotating spherical shells. In physical systems such as the Earth's core, a fixed heat-flux applies to the outer boundary and we study the effect of applying large scale lateral heat-flux heterogeneities. For uniform heat-flux, thermal onset occurs at a critical Rayleigh number, $R_c$, with flow of a characteristic wavenumber, $m_c$. The fixed-flux boundary condition favours large scale ($m_c = 1$) flows to lower Ekman numbers, $E$, than the fixed temperature condition. $m_c = 1$ flows are preferred to lower $E$ for high Prandtl numbers, $P_r$, and rigid boundaries. We present a nonlinear drifting solution to the uniform heat-flux boundary problem which shows a longitudinal asymmetry: one hemisphere displays large scale toroidal flow whilst the opposite hemisphere displays smaller scale thermal convection. We then change the boundary heat-flux to vary laterally as the spherical harmonic $Y_2^2(\theta, \phi)$, with strength measured by $\epsilon$. Flow now occurs for all non-zero Rayleigh numbers, $R$, and is steady for $R < R_c$. We look at

† Current address: Institutt for geologi, Postboks 1047 Blindern, N-0316 Oslo, Norway.

time-dependent convection with $R > R_c$ for two sets of parameters which prefer different forms of convection at onset. At $P_r = 0.6$, both thermal convection and boundary-driven flow display $m = 2$ symmetry and, for low $\epsilon$, periodic flows of the same symmetry are observed. At higher $\epsilon$, the symmetry is broken as odd $m$ are excited. For $P_r = 6.0$, $m = 1$ is preferred for uniform heat-flux and, for low $\epsilon$, $m = 1$ and $m = 2$ modes compete. Higher $\epsilon$ suppresses the $m = 1$ mode and an $m = 2$ symmetry is imposed by the boundary.

## 1. Introduction

The Earth's fluid outer core is surrounded by a viscous mantle which convects on a far longer time-scale. The thermal structure of the lower-most mantle will persist for great lengths of time, over which the relatively rapid motion of molten iron in the core will act to maintain an isothermal core-mantle boundary (CMB). Convection in the mantle is therefore subjected to a uniform temperature boundary condition at the CMB and core fluid will experience a constant heat-flux at the same interface. Mantle convection will lead to (possibly large) lateral temperature variations within the thermal boundary layer directly above the CMB. This will result in lateral heat-flux inhomogeneity at the CMB with consequences for the outer-core flow and magnetic field morphology (Gubbins & Richards 1986; Bloxham & Gubbins 1987). Long term mantle control over core processes is indicated by persistent non-axisymmetric features in the historical (Bloxham, Gubbins & Jackson 1989; Hutcheson & Gubbins 1990) and paleomagnetic (Gubbins & Kelly 1993; Johnson & Constable 1995) records. In principle, the spatial structure of temperature variations in the lower-most mantle can be determined from lateral seismic velocity variations, with secondary or S-wave velocities likely to be the best indicator (Karato 1993; Stacey 1995, 1998). Relatively low (high) S-wave velocity is likely to correspond to relatively high (low) temperature. Long wavelength heterogeneities are likely to dominate

(see, for example, Su & Dziewonski 1991; Masters *et al.* 1996) and the shear-velocity models of Masters *et al.* (1996) and others (reviewed by Masters & Shearer 1995) indicate that the largest component of the S-wave variation is a $Y_2^2(\theta, \phi)$ spherical harmonic (see §2 for definition).

Thermally driven convection of fluid in rotating spheres and spherical shells is fundamental to the fluid dynamical systems which generate the magnetic fields of the Earth and other planetary bodies. Numerous studies address the onset of thermal instability (Chandrasekhar 1961; Roberts 1968; Busse 1970; Zhang & Busse 1987; Yano 1992; Zhang & Jones 1993; Ardes, Busse & Wicht 1997; Jones, Soward & Mussa 2000) and finite amplitude convection (Zhang 1991, 1992; Sun, Schubert & Glatzmaier 1993; Tilgner & Busse 1997) in spherical geometry. All of these studies assume the boundary to be a perfect thermal conductor, and so fix a uniform temperature at the outer surface. Zhang & Gubbins (1993) demonstrated how, in the absence of a magnetic field, relatively small variations in the temperature imposed at the outer surface can lock the convection rolls to the surface heterogeneity. For other parameters, the resulting flow was found to vascillate between length scales fixed by the boundary temperature and those preferred by the uniform-boundary convection. Inertia was found, by Zhang & Gubbins (1996), to lessen the ability of the boundary to lock flow. For numerical simplicity, these studies fixed the temperature and not the heat-flux at the outer boundary.

However, several studies (Dormy 1997; Gibbons 1998; Takehiro *et al.* 1999) have established examples of systems where fixing the heat-flux, as opposed to the temperature, leads to very different behaviour at onset of thermal instability. For rotation rates which, given fixed temperature boundaries, would lead to marginally stable convection in the form of many small length-scale drifting cells, the fixed flux boundary condition favours large scale flows with a single upwelling and downwelling. It may therefore transpire that

the effect on convective instability of a non-uniform heat-flux may be somewhat different to that of a heterogeneous temperature boundary. This paper addresses this problem.

Inhomogeneous cooling at the outer surface of rotating spherical fluid shells has been the subject of several further numerical investigations. Sun, Schubert & Glatzmaier (1994) applied different patterns of lateral temperature heterogeneities to highly supercritical thermal convection. Lateral variations in the outer-boundary heat-flux have been applied in the contexts of magnetoconvection (Olson & Glatzmaier 1996) and self-consistent dynamo simulations (Glatzmaier & Roberts 1997; Sarson, Jones & Longbottom 1997; Bloxham 2000). The systems in all of these studies are strongly nonlinear and time-dependent and the numerical simulations are correspondingly expensive. As a result, a very limited range of parameters can be explored. Examining the behaviour close to onset allows the fundamental effect of changing the thermal boundary condition to be understood over a wide range of parameters.

Before performing calculations with heterogeneous cooling, we determine the onset thermal instability for the uniform heat-flux problem. The effect of changing the outer boundary condition from fixed temperature to fixed heat-flux was explored by Gibbons (1998) who examined the onset of convection, for both boundary conditions, in spherical shells of different radius ratio, at infinite Prandtl number and with uniform heat sources throughout the shell. Dormy (1997) compared the onset of convection in systems with uniform heat sources and fixed temperature outer boundary to those with no internal heating and fixed heat-flux at the outer boundary, all at $P_r = 1$. Takehiro *et al.* (1999) briefly examined onset of convection in spherical geometry in a study which primarily addressed the effect of fixed-flux boundaries on thermal instability in a rotating cylindrical annulus. In §3, we illustrate and expand upon the principal results of these three studies.

In §4, we solve the nonlinear problem with uniform heat-flux at the outer boundary. We then apply a lateral variation in the outer-surface heat-flux and solve for steady flows (§5). We test the validity of all such boundary-locked solutions with linear stability analysis. In §6, where we find that the steady solutions are unstable, we solve the full equations with a time-step code.

## 2. Mathematical and numerical formulation

In the following treatment, $r$, $\theta$ and $\phi$ denote the standard spherical polar coordinates and $\boldsymbol{r}$ is the position vector. A spherical fluid shell rotates with a constant angular velocity, $\Omega$, and has inner and outer radii $r_{\rm i}$ and $r_{\rm o}$ respectively. Gravity within the shell is given by

$$\boldsymbol{g} = -\gamma \boldsymbol{r}, \tag{2.1}$$

where $\gamma$ is a constant. The thermal expansivity, $\alpha$, thermal diffusivity, $\kappa$, and viscosity, $\nu$, are all constant throughout the shell. A basic state temperature, $T_s$, is maintained by a uniform distribution of heat sources such that

$$\nabla T_s = -\beta \boldsymbol{r}, \tag{2.2}$$

for constant $\beta$ (see for example Roberts 1968; Busse 1970). The velocity, $\boldsymbol{v} = (v_r, v_\theta, v_\phi)$, and temperature perturbation from $T_s$, denoted by $T$, are related by the Navier-Stokes equation

$$\left(\frac{\partial}{\partial t} + \boldsymbol{v}.\nabla\right)\boldsymbol{v} + 2\Omega \boldsymbol{k} \times \boldsymbol{v} = -\nabla \tilde{p} + \alpha\gamma T \boldsymbol{r} + \nu \nabla^2 \boldsymbol{v} \tag{2.3}$$

and the heat equation

$$\frac{\partial T}{\partial t} + \boldsymbol{v}.\nabla T = \kappa \nabla^2 T + \beta \boldsymbol{v}.\boldsymbol{r}, \tag{2.4}$$

where $\boldsymbol{k}$ is a unit vector aligned with the rotation axis. The term $\nabla\tilde{p}$ is the force due to the pressure gradient and is removed from the problem by taking the curl of Equation (2.3).

Scaling length by $d = r_{\rm o} - r_{\rm i}$, time by $d^2/\kappa$ (the thermal diffusion time) and temperature by $d^2/\beta$ respectively allows equations (2.3) and (2.4) to be written in the dimensionless forms

$$P_r^{-1}\left(\frac{\partial}{\partial t} + \boldsymbol{v}.\nabla\right)\boldsymbol{v} + E^{-1}\boldsymbol{k}\times\boldsymbol{v} = -\nabla\tilde{p} + RT\boldsymbol{r} + \nabla^2\boldsymbol{v} \tag{2.5}$$

and

$$\frac{\partial T}{\partial t} + \boldsymbol{v}.\nabla T = \nabla^2 T + \boldsymbol{v}.\boldsymbol{r}. \tag{2.6}$$

The problem is now controlled by the Prandtl number, $P_r$, the Rayleigh number, $R$, and the Ekman number, $E$, given respectively by

$$P_r = \frac{\nu}{\kappa},\ R = \frac{\alpha\beta\gamma d^6}{\nu\kappa},\ \text{and}\ E = \frac{\nu}{2\Omega d^2}. \tag{2.7}$$

The aspect ratio $\eta = r_{\rm i}/r_{\rm o}$ is set to 0.4 in the majority of calculations, being close to the value for Earth ($\eta_E \approx 0.351$) and allowing direct comparisons with previous work. In the Boussinesq approximation, $\boldsymbol{v}$ is divergence free,

$$\nabla.\boldsymbol{v} = 0, \tag{2.8}$$

and so the velocity field can be expanded in toroidal and poloidal vectors;

$$\boldsymbol{v} = \nabla\times(\ w(r,\theta,\phi)\boldsymbol{r}\ ) + \nabla\times\nabla\times(\ v(r,\theta,\phi)\boldsymbol{r}\ ). \tag{2.9}$$

The impenetrable condition at the boundaries requires that

$$v(r_{\rm i}) = v(r_{\rm o}) = 0. \tag{2.10}$$

The additional constraints on the velocity are

$$\left.\frac{\partial^2 v}{\partial r^2}\right|_{r_{\rm i},r_{\rm o}} = \left.\frac{\partial}{\partial r}\left(\frac{w}{r}\right)\right|_{r_{\rm i},r_{\rm o}} = 0 \tag{2.11}$$

for the case of stress-free boundaries and

$$\left.\frac{\partial v}{\partial r}\right|_{r_i,r_o} = \left. w \right|_{r_i,r_o} = 0 \tag{2.12}$$

when the boundaries are rigid. Imposing a thermal heterogeneity at the outer surface means imposing either

$$T(r_o,\theta,\phi) = \mathcal{T} g(\theta,\phi), \tag{2.13}$$

for fixed temperature, or

$$\left.\frac{\partial T(\theta,\phi)}{\partial r}\right|_{r_o} = -\mathcal{A} g(\theta,\phi), \tag{2.14}$$

for fixed heat-flux. In this paper we fix the heat-flux, $-\partial T/\partial r$, for most of the calculations, and fix the temperature, $T$, for a few comparison solutions and to benchmark the numerical code against the results of Zhang & Gubbins (1993, 1996). The most straightforward way to implement this is to decompose the temperature, $T$, into a homogeneous part, $\Theta$, and a fixed inhomogeneous part, $fg$, with

$$T = \Theta(r,\theta,\phi,t) + \epsilon f(r) g(\theta,\phi). \tag{2.15}$$

The heterogeneity function $g(\theta,\phi)$ is normalised with the condition

$$\int_0^{2\pi}\int_{-\pi}^{\pi} \left[g(\theta,\phi)^2\right] \sin\theta d\theta d\phi = 1 \tag{2.16}$$

and has a zero spherical average. In the fixed heat-flux calculation, the strength of the lateral heat-flux variation relative to the mean radial heat-flux is controlled by $\epsilon$ with

$$\epsilon = \frac{\mathcal{A}}{\beta d}. \tag{2.17}$$

The corresponding parameter in the fixed temperature calculation is given by

$$\epsilon_T = \frac{\mathcal{T}}{\beta d^2}. \tag{2.18}$$

For calculations with fixed heat-flux at the outer boundary,

$$\left.\frac{\partial \Theta}{\partial r}\right|_{r_o} = 0, \quad \left.\frac{df}{dr}\right|_{r_o} = -1 \tag{2.19}$$

and, for fixed $T$,

$$\Theta(r_{\rm o}) = 0, \qquad f(r_{\rm o}) = 1. \tag{2.20}$$

The temperature is fixed and uniform at the inner boundary in all cases;

$$\Theta(r_{\rm i}) = 0, \qquad f(r_{\rm i}) = 0. \tag{2.21}$$

The scalar functions $g(\theta,\phi)$, $\Theta(r,\theta,\phi)$, $w(r,\theta,\phi)$ and $v(r,\theta,\phi)$ are expanded in series of spherical harmonics, truncated at degree $l = L$,

$$g(\theta,\phi) = \sum_{l=1}^{L}\sum_{m=0}^{l} \left[g_l^{mc}\cos m\phi + g_l^{ms}\sin m\phi\right] P_l^m(\cos\theta) \tag{2.22}$$

$$\Theta(r,\theta,\phi) = \sum_{l=0}^{L}\sum_{m=0}^{l} \left[\Theta_l^{mc}(r)\cos m\phi + \Theta_l^{ms}(r)\sin m\phi\right] P_l^m(\cos\theta) \tag{2.23}$$

$$w(r,\theta,\phi) = \sum_{l=1}^{L}\sum_{m=0}^{l} \left[w_l^{mc}(r)\cos m\phi + w_l^{ms}(r)\sin m\phi\right] P_l^m(\cos\theta) \tag{2.24}$$

$$v(r,\theta,\phi) = \sum_{l=1}^{L}\sum_{m=0}^{l} \left[v_l^{mc}(r)\cos m\phi + v_l^{ms}(r)\sin m\phi\right] P_l^m(\cos\theta) \tag{2.25}$$

where the associated Legendre functions, $P_l^m(\cos\theta)$, are Schmidt quasi-normalised with

$$\int_{-\pi}^{\pi} \left[P_l^m(\cos\theta)\right]^2 \sin\theta d\theta = \frac{2(2-\delta_{m0})}{2l+1}. \tag{2.26}$$

The spherical harmonics $Y_l^{mc}$ and $Y_l^{ms}$ are respectively defined by

$$Y_l^{mc}(\theta,\phi) = P_l^m(\cos\theta)\cos(m\phi) \tag{2.27}$$

and

$$Y_l^{ms}(\theta,\phi) = P_l^m(\cos\theta)\sin(m\phi). \tag{2.28}$$

At the onset of convection, with $\epsilon = 0$, the nonlinear terms in equations (2.5) and (2.6) are neglected and modes decouple in $m$, although the Coriolis force still couples terms in $l$. In addition, the equatorially symmetric ($E^S$) components with

$$(v_r, v_\theta, v_\phi)(r,\theta,\phi) = (v_r, -v_\theta, v_\phi)(r,\pi-\theta,\phi) \tag{2.29}$$

and the equatorially anti-symmetric ($E^A$) components with

$$(v_r, v_\theta, v_\phi)(r, \theta, \phi) = (-v_r, v_\theta, -v_\phi)(r, \pi - \theta, \phi) \tag{2.30}$$

can be treated separately. Busse (1970) showed the $E^S$ components to be the physically realised solutions and so only they are dealt with here.

The functions $\Theta$, $v$ and $w$ are treated as perturbations with exponential time-dependence $\partial/\partial t = \sigma = \sigma_r + i\sigma_i$. The resulting eigenproblem,

$$P_r^{-1} \nabla \times \sigma \boldsymbol{v} = -E^{-1} \nabla \times (\boldsymbol{k} \times \boldsymbol{v}) + R \nabla \times \Theta \boldsymbol{r} + \nabla \times \nabla^2 \boldsymbol{v} \tag{2.31}$$

$$\sigma \Theta = \nabla^2 \Theta + \boldsymbol{v}.\boldsymbol{r}, \tag{2.32}$$

subject to the formulation of equations (2.23) to (2.25), forms a set of coupled ordinary differential equations in $r$.

The radial functions for $\Theta$, $v$ and $w$ are represented at $N$ arbitrarily spaced grid nodes and derivatives are calculated by finite difference methods. Positioning the grid nodes at the zeros of the Chebyshev polynomial $T_N$, scaled over the interval $(r_\mathrm{i}, r_\mathrm{o})$, was found to give far better accuracy for computational cost than the same number of equally spaced nodes. This non-equidistant grid spacing has more nodes concentrated close to the boundaries, where there is the greatest need for good resolution. When stress-free boundaries are used, the frame of reference in which solid body rotations vanish is employed.

At the onset of thermal instability the perturbations do not decay and $\sigma_r = 0$, the corresponding value of $R$ called the critical Rayleigh number, $R_c$. The mode $m$ possessing the lowest value of $R_c$ is called the critical wavenumber, $m_c$. It must be verified that every $R_c$ calculated is essentially independent of the numerical resolution, controlled by the integer parameters $L$ and $N$. Table 1 shows how the critical Rayleigh numbers for selected $m$ vary with numerical resolution at the switchover between $m_c = 1$ and

$m_c = 11$ for rigid boundaries, infinite Prandtl number and $E \approx 1.4 \times 10^{-4}$. If the numerical resolution is insufficient, the wrong critical wavenumber, $m_c$, is chosen.

The eigenvalues, $\sigma$, to the eigensystem in equations (2.31) and (2.32) are found using the implicitly restarted Arnoldi method (Lehoucq, Sorensen & Yang 1998; Arnoldi 1951; Sorensen 1992). This method returns several eigenvalues and can utilise the banded structure of the matrix which results from the short-range interactions of the finite difference method for radial derivatives.

When $\epsilon$ is non-zero there is no critical regime. For any non-zero Rayleigh number, a flow will be forced by the lateral variation in heat-flux (see Zhang & Gubbins 1992; Gibbons & Gubbins 2000). At sub-critical $R$, in the absence of convective instability, this flow is likely to be steady and we may solve for a nonlinear solution to equations (2.5) and (2.6) with $\partial/\partial t = 0$ by Newton-Raphson iteration. As a result of the nonlinear terms, the spherical harmonics no longer decouple in $m$. Therefore, despite the banded structure of the Jacobian matrix which results from the finite difference scheme for radial derivatives, the memory requirements for these calculations rapidly increase with $L$. For regions of parameter space where the Newton-Raphson method is impractical, it is more efficient to use a time-stepping code to converge towards a steady solution when a non-uniform boundary temperature or heat-flux is imposed. The time-stepping and Newton-Raphson codes were written independently and the use of both codes provides a useful check on the validity of the solutions obtained.

The validity of any such steady solution, $(\boldsymbol{v}_0, \Theta_0)$, must be determined by a linear stability analysis. The steady solution is subjected to a perturbation, $(\tilde{\boldsymbol{v}}, \tilde{\Theta})$, with

$$\boldsymbol{v} = \boldsymbol{v}_0 + \tilde{\boldsymbol{v}} \tag{2.33}$$

and

$$\Theta = \Theta_0 + \tilde{\Theta}. \tag{2.34}$$

An exponential time dependence of the form $\partial/\partial t = \sigma$ is assumed for $\tilde{\boldsymbol{v}}$ and $\tilde{\Theta}$, resulting in the eigenvalue problem

$$\begin{aligned} \sigma P_r^{-1} \nabla \times \tilde{\boldsymbol{v}} &= -P_r^{-1} \nabla \times [(\boldsymbol{v}_0.\nabla)\tilde{\boldsymbol{v}} + (\tilde{\boldsymbol{v}}.\nabla)\boldsymbol{v}_0] \\ &\quad -E^{-1} \nabla \times (\boldsymbol{k} \times \tilde{\boldsymbol{v}}) + R \nabla \times (\tilde{\Theta} \boldsymbol{r}) + \nabla \times \nabla^2 \tilde{\boldsymbol{v}} \\ \sigma \tilde{\Theta} &= \tilde{\boldsymbol{v}}.\boldsymbol{r} - \boldsymbol{v}_0.\nabla \tilde{\Theta} - \tilde{\boldsymbol{v}}.\nabla(\Theta_0 + \epsilon f g) + \nabla^2 \tilde{\Theta}. \end{aligned} \tag{2.35}$$

The eigenvalue $\sigma = \sigma_{\rm r} + i\sigma_{\rm i}$ is, in general, complex and an eigenvalue with real part $\sigma_{\rm r} < 0$ indicates that the steady solution is stable to perturbation and the steady solution is valid. An eigenvalue with $\sigma_{\rm r} > 0$ indicates that the perturbation will grow; and the solution is therefore unstable. A full time integration is then needed to follow the evolution of the flow and temperature. A linearized time-stepping code can be used to calculate growth rates of perturbations if the memory requirements are too great for the eigenvalue problem to be practical. Again, the linear stability code provides good validation for the time-dependent code.

We have high confidence in the validity of the uniform thermal boundary solutions as a result of the excellent agreement between the present time-stepping code and several other independently developed codes in the convection and dynamo benchmark study of Christensen *et al.* (2000). The non-uniform boundary code has only minor modifications from the benchmarked code. A semi-implicit Crank-Nicolson scheme was used to time-step the diffusive terms in the heat and momentum equations. The velocity, $\boldsymbol{v}$, the vorticity, $\nabla \times \boldsymbol{v}$, and temperature gradient, $\nabla T$, are transformed into $(r, \theta, \phi)$-space at each time step, using a Fast Fourier Transform in the $\phi$ direction and alias-free Gaussian quadrature in the $\theta$ direction. The nonlinear terms are evaluated in real space and a predictor-corrector iterative method is used to solve for $\boldsymbol{v}$ and $\Theta$ at the next time-step.

## 3. Onset of thermal convection with uniform heat-flux at the outer boundary

With fixed temperature boundaries and infinite Prandtl number, the critical wavenumber increases with rotation speed. For rigid boundaries, the increase in $m_c$ is monotonic. In the case of stress-free boundaries, there is an anomalous switchover from $m_c = 8$ to $m_c = 7$ at $E \approx 10^{-3}$ (see table 2 for details). This discrepancy aside, the observed increase is similar to that reported throughout the literature. At high rotation speeds, the Coriolis force dominates and the flow attempts to align with the rotation axis in order to satisfy the Proudman-Taylor theorem. Due to the curvature of the boundaries, $\partial \boldsymbol{v}/\partial z$ (where $z = r\cos\theta$) can never entirely vanish and the rotational constraint must be broken by the viscous effect. This is achieved by reducing the horizontal length scale of the flow.

Figure 1 shows critical Rayleigh numbers for several $m$ in the fixed heat-flux, infinite Prandtl number case with stress-free boundaries. The fixed-flux boundary condition promotes instability of the $m = 1$ mode at far lower values of $E$ than is found for fixed temperature boundaries. The mode possessing the lowest critical Rayleigh number varies with $E$ in a similar way to that reported in previous works (for example Zhang & Busse 1987) with the exception of the $m = 1$ mode. To cast light upon the anomalous preference for $m = 1$ with fixed flux, we examine streamlines of flow and temperature contours, in the equatorial plane, for $m = 1$ and $m = 4$ at onset (figure 2). We note that $m = 4$ is the preferred wavenumber for convection at $E = 10^{-2}$ for the fixed temperature outer boundary condition. In the fixed heat-flux system, the temperature at the outer boundary is constrained only by the geometry of the system and the preferred mode of convection maintains a lateral temperature gradient which penetrates deep into the shell, facilitating a very large scale flow for optimal heat transport. Under the alternative fixed

$T$ boundary condition, these lateral temperature gradients would vanish at the boundary and this large scale flow would be inhibited by the effects of rotation. For larger wavenumbers (e.g. $m = 4$), the smaller ratio of lateral to vertical length scale means that the effect of the thermal boundary condition is diminished, which explains the pattern observed for higher $m$ in figure 1. At $E = 10^{-3}$, in the lower part of figure 2, the rotation effects have become dominant and the strongest lateral temperature gradients have been driven deeper into the shell. The streamlines of flow now tend to follow, and not cross, the contours of constant temperature and the $m = 1$ mode no longer offers the most effective heat transport.

At Ekman numbers lower than those shown in figure 1, the relationship between $m_c$ and $E$ is very similar to that for fixed temperature and the importance of the thermal boundary condition diminishes. Figure 3 shows almost no difference between the form of flow in the preferred mode at $E = 3.162 \times 10^{-4}$ for the two boundary conditions, flow being concentrated towards the inner region of the shell.

The behaviour is even more surprising for rigid boundaries, with the large length-scale flow preferred for Ekman numbers as low as $E \approx 1.4 \times 10^{-4}$. The preferred mode changes from $m_c = 3$ to $m_c = 2$ at $E \approx 5 \times 10^{-3}$ and again from $m_c = 2$ to $m_c = 1$ at $E \approx 1.05 \times 10^{-3}$. At lower $E$, $m = 1$ is replaced with the far smaller length-scale $m = 11$ flow as the preferred mode. (The numerical convergence of the solutions on either side of this transition is demonstrated in table 1.) Because of the wide range of $E$ over which the anomalous behaviour of critical mode selection occurs, the corresponding range of $R_c$ is very large and plotting $R_c$ against $E$ for the individual wavenumbers (as in figure 1) would show little detail of the switchovers. Roberts (1968) showed that $R_c$ would be proportional to $E^{-4/3}$ in the limit of small Ekman number, and so figure 4 shows the critical Rayleigh numbers for selected wavenumbers scaled by $E^{4/3}$ against $E$.

Figure 5 indicates how, at $E = 10^{-2}$, both the $m = 1$ and $m = 2$ modes exhibit large lateral temperature variations which penetrate deep into the shell. However, the larger scale $m = 1$ flows are required (by the geometry of the $\eta = 0.4$ spherical shell) to have proportionately more contact with the flow-inhibiting rigid boundaries than the $m = 2$ convecting cells, favouring the latter. (Gibbons 1998, shows that for the deeper $\eta = 0.2$ shell, the $m = 1$ mode meets less resistance from the boundaries and is consequently preferred at these rotation rates.) For $E = 3.152 \times 10^{-4}$, the $m = 2$ mode is inhibited as the greater influence of the Coriolis force has driven the lateral temperature gradients deeper into the shell (lower part of figure 5). The larger scale $m = 1$ flow is less effective at breaking up the lateral temperature gradients close to the boundaries than the smaller convective cells and is once more the preferred mode of heat transport.

Having established the result for infinite Prandtl number, it is necessary to explore the extent of its validity for finite $P_r$. At small $P_r$, inertial effects dominate over thermal and the behaviour of $T$ at the boundaries would be expected to be less significant. The study of Dormy (1997) also found the $m = 1$ mode to be preferred at moderate Ekman number ($E = 3.1623 \times 10^{-4}$) in a system with no internal heat sources, $\eta = 0.35$ and $P_r = 1$. This suggests that the thermal boundary condition is of greater importance than the mode of heating for the selection of a critical mode in this parameter regime.

Critical wavenumbers and Rayleigh numbers were sought for finite $P_r$ over the ranges $10^{-3/2} \geq E \geq 2 \times 10^{-4}$ (stress-free boundaries) and $10^{-3/2} \geq E \geq 7 \times 10^{-5}$ (rigid boundaries). At Ekman numbers lower than these limits, no preference for large length-scale flows had been found and it can be expected that the $R_c$ and $m_c$ will follow asymptotic behaviour as a function of $E$ (see, for example, Zhang 1991). For $P_r = 10$, the behaviour is very similar to the infinite Prandtl number case and it was deemed unnecessary to consider finite $P_r$ greater than 10. Figure 6 illustrates how the critical wavenumber, $m_c$,

varies as a function of $P_r$ and $E$ for both stress-free and rigid boundaries. The sketch is based on 17 different $P_r$ values with $P_r \geq 0.1$ and each subsequent value being a factor $10^{1/8}$ greater than the previous. This inevitably means that some degree of interpolation has been employed to construct the lines. With some features, however, such as the multiple crossovers between wavenumbers 5 and 6 for stress-free boundaries, or the sudden changes from small to large $m_c$, special care was taken to ensure that boundaries were numerically well-resolved.

The $m = 1$ mode is preferred over a far greater range of $E$ for rigid boundaries than for stress-free as the rigid boundaries inhibit flow near to the surface, which acts to produce a more uniform boundary temperature. At lower Prandtl number, the range of $E$ over which the large length-scale flows are preferred is smaller for both stress-free and rigid boundary systems.

## 4. Finite amplitude convection with uniform heat-flux imposed at the outer boundary.

Reinstating the nonlinear terms into the Navier-Stokes and heat equations allows us to solve for time-dependent solutions at super-critical Rayleigh numbers. Wavenumbers do not decouple and we investigate the interaction of the large length scale ($m = 1$) flow, preferred by the uniform heat-flux boundary, with the smaller scale cells, which are preferred at larger Rayleigh numbers. With parameters where $m = 1$ instabilities are preferred (see figure 6) the nonlinear solutions are predictably dominated by $m = 1$ components, when the Rayleigh number is not greatly above critical. Other wavenumbers add small contributions to the flow by virtue of the nonlinear interactions.

Increasing $R$ will excite higher wavenumbers. Figure 7 displays a solution with $E = 2.8 \times 10^{-3}$, $P_r = 10$, $R = 4900$ and stress-free boundaries. The kinetic energy in the

flow stays constant and the only time-dependence (figure 7 a) is a steady prograde drift in longitude. The solution repeats itself every 1.251 thermal diffusion times. Although the picture is somewhat complicated by the appearance of several small scale convection cells in some regions of the shell, figure 7 (e) shows that, fundamentally, one hemisphere has above average temperature at the equator whilst the temperature of the opposite hemisphere is below average; consistent with a dominant $m = 1$ component. In figure 7 (d), a large length scale toroidal flow is moving retrograde relative to the drifting frame from the region of greatest temperature to that of lowest temperature. The contours for $v_r$ (figure 7 c) show that the region occupied by this westward flow contains almost no radial velocity, the remaining region of the sphere containing convection rolls with a length scale consistent with an $m = 4$ or $m = 5$ flow. In the small scale convective region, $v_\phi$ is positive (eastward). The hemispherical asymmetry of this solution is most clearly seen in figure 7 (b).

In other regions of parameter space, where the most unstable wavenumber is $m = 1$ and where the second most unstable mode has a much larger $m$, steadily-drifting solutions were obtained which showed similar characteristics to the solution displayed in figure 7. The preferred mode has a large horizontal length-scale but, at higher $R$, convection with a much smaller length-scale is excited which co-exists in nonlinear interaction with the underlying $m = 1$ flow. The resulting system has an 'East-West' hemispherical asymmetry.

At higher values of $R$, the effects of the large scale flow are still seen although the simple time-dependence, which allows us to examine the effect of the fixed-flux boundary condition so closely, is lost.

## 5. Solutions locked by a heat-flux inhomogeneity at the outer boundary

We now study the effect of imposing a $Y_2^2$ lateral heat-flux variation at the outer surface. We investigate two regions of parameter space with a moderate Ekman number, $E = 5 \times 10^{-3}$, where the velocity satisfies stress-free boundary conditions. For the uniform ($\epsilon = 0$) heat-flux problem, $m = 2$ and $m = 1$ are the most unstable wavenumbers for Prandtl numbers 0.6 and 6.0 respectively (see figure 6). Table 3 shows critical Rayleigh numbers for equatorially symmetric modes $m = 1$ to $m = 6$ for these values.

In the absence of unstable thermal convection, a pattern of lateral cooling, $g(\theta, \phi)$, forces a flow ($\boldsymbol{v}_0$) and temperature distribution ($\Theta_0$). Since $g(\theta, \phi)$ satisfies

$$g(\theta, \phi) = g(\theta, \pi + \phi), \tag{5.1}$$

the expansions which represent the solution, $(\boldsymbol{v}_0, \Theta_0)$, need only contain wavenumbers, $m$, which satisfy $m = 2n$, for non-negative integers $n$ (see Gubbins & Zhang 1993, for details on the symmetry properties of equations 2.3 and 2.4). This forced convection is a thermal wind type flow and exists for any non-zero Rayleigh number and non-zero $\epsilon$. In the absence of a critical regime for the onset of flow in the non-uniform heat-flux boundary problem, we continue to refer to the critical Rayleigh number, $R_c$, as the Rayleigh number necessary for the onset of thermal instability with a uniform-flux boundary. Figure 8 shows a typical steady flow at sub-critical Rayleigh number, driven by the thermal heterogeneity on the boundary. Upwelling occurs not under the warmest part of the boundary (as would be expected in a non-rotating system) but where, moving in the direction of rotation, the outward heat-flux changes from below average to above average. In the absence of convection heated from below, this would appear to be the

how the boundary-driven flow will behave as the Ekman number decreases Gibbons & Gubbins (2000).

Provided the Rayleigh number stays subcritical, the form of the forced convection does not change greatly as a function of $\epsilon$, $R$ and $P_r$. The kinetic energy of the flow, however, increases strongly with both $R$ and $\epsilon$. Using a $Y_4^4$ spherical harmonic lateral variation of surface temperature, Zhang & Gubbins (1993) found two temperature layers to form as $R$ was increased. This was due to the emergence of convection rolls with the same lateral length scale as the imposed thermal heterogeneity. Such a phenomenon was not observed here, probably due to the much larger length scale ratio of the surface heating anomaly to the depth of the shell for the $Y_2^2$ harmonic.

We must now consider the stability of the boundary driven flows. As a result of the symmetry of the steady flow, two classes of perturbation, $(\tilde{\boldsymbol{v}}, \tilde{\Theta})$, may be considered separately. They are characterised by the Floquet integers $M = 0$ and $M = 1$, containing only wavenumbers, $m$, with $m = 2j + M$ (see Zhang & Gubbins 1993) where $j$ are non-negative integers. Figure 9 shows the lines of critical stability for both classes of perturbation for $P_r = 0.6$ and $P_r = 6.0$. For a given $\epsilon$, $R_s(M)$ is defined as the lowest value of $R$ for which a perturbation of class $M$ achieves a growth rate with a zero real part. The minimum value of $R_s(0)$ and $R_s(1)$ is simply denoted $R_s$. The steady solution, $(\boldsymbol{v}_0, \Theta_0)$, is valid only for $R < R_s$ or, alternatively, the points in figures 9 (a) and 9 (b) which lie to the left of both of these lines.

For both cases studied, the strength of the boundary heating heterogeneity needs to be quite large before the flow is boundary-locked at Rayleigh numbers significantly above critical. For low $\epsilon$ and $P_r = 0.6$ (figure 9 a), the stability boundary is controlled by the $M = 0$ class of perturbations which contain only even $m$. However, as $\epsilon$ is increased, far higher Rayleigh numbers are required to destabilise the locked flow to the $M = 0$

perturbations. The effect of increasing the strength of the $Y_2^2$ boundary heating has a lesser effect on the stability to $M = 1$ perturbations and, paradoxically, increasing the strength of a $\cos 2\phi$ mode leads to the solution becoming unstable to a class of perturbations containing only odd wavenumbers.

In the $P_r = 6.0$ case (figure 9 b), the $m = 1$ mode is far more unstable than the larger wavenumbers in the uniform boundary problem and, predictably, the $Y_2^2$-locked solution becomes unstable to $M = 1$ class perturbations for moderate values of $\epsilon$. The ability of the surface heat-flux variation to lock the flow increases substantially with $\epsilon$. At $\epsilon \approx 0.54$, a different mode of instability, belonging to the $M = 0$ class of perturbations, takes over. At this point, the symmetry imposed by the surface heating takes precendence over the symmetry preferred by the heterogeneously cooled system.

For all parameters examined, the eigenvalues corresponding to the perturbation growth rates had non-zero imaginary part. Beyond the stability boundary, $R = R_s$, the time-derivatives in equations (2.5) and (2.6) cannot be omitted and the nonlinear solutions must be solved by a time-stepping procedure.

## 6. Time-dependent flows subject to a laterally varying heat-flux at the outer boundary

Figure 9(a) shows that, for $P_r = 0.6$ and the other parameters described in §5, $\epsilon = 0.30$ is almost the largest lateral heat-flux variation for which the stability boundary is controlled by the $M = 0$ class of perturbation. $R = 1200$ is approximately 5% beyond the $R_s$ stability boundary for $P_r = 0.6$, $E = 5 \times 10^{-3}$ and $\epsilon = 0.30$ for stress-free fluid boundaries. We note that for $\epsilon = 0$ and $R = 1200$, the finite amplitude solution drifts steadily prograde with most kinetic energy in the wavenumber $m = 2$, but with other even $m$ contain small components due to nonlinear interactions. Time-stepping with

$\epsilon = 0.30$, from an initial condition containing the boundary-driven solution and additional perturbations of all symmetries, leads to a periodic flow containing only components with $m$ even. However large the initial perturbations with odd $m$, they will ultimately decay given a sufficiently long integration time.

Figure 10 shows the variation of kinetic energy of flow components throughout one half-cycle. After an initial energy maximum, where the solution resembles the predominantly boundary-driven flow in figure 8, the system attempts to propagate in the direction of rotation. In both the drifting ($\epsilon = 0$) and steady thermal-wind (non-zero $\epsilon$) solutions, the flow and temperature distribution maintain a constant phase relationship. In this time-dependent system, this relationship is made impossible by the propagation of the flow relative to the boundary heat-flux variation. The kinetic energy begins to diminish and the isotherms distort (figure 10 a), with the large upwelling then splitting into two (figure 10 b). The kinetic energy of the dominant $m = 2$ component decreases dramatically (almost two orders of magnitude) until it is dominated by the $m = 4$ mode, which is less suppressed as a result of its smaller horizontal length scale. Figure 10 (c) shows the emergence of these smaller convection cells despite the clear larger length scale of the temperature variations. The small scale cells are able to propagate past the surface heat-flux heterogeneity more readily and the large scale flow reforms (figure 10 d) in the same flow-temperature phase observed at the previous kinetic energy maximum. Large length scale thermal forcing for parameters which, given uniform thermal boundaries, would naturally prefer large scale flows have resulted in a solution which alternates between large and small length scales depending upon the phase between the boundary heterogeneity and the convection rolls.

With $\epsilon = 0.4$, and otherwise the same parameters, figure 9 (a) shows that the stability of the $Y_2^2$ boundary-driven flow is now determined by the $M = 1$ class of perturbations.

Figure 11 shows variation of the kinetic energy with time for the integration of the full nonlinear equations. Although some regular fluctuation occurs, it is within a few percent of a time-averaged value and not the two orders of magnitude variation observed for the weaker $\epsilon = 0.3$ case. The strong $\cos 2\phi$ heating mode keeps the solution dominated by the $m = 2$ wavenumber, although components with $m$ odd do not decay with time. The $m = 3$ flow components consistently maintain approximately one order of magnitude less kinetic energy than the $m = 2$ components, although this additional symmetry-breaking element of the flow clearly facilitates the drift of the solution past the surface thermal heterogeneity.

We now consider solutions with $P_r = 6.0$. Table 3 shows the critical Rayleigh number for $m = 1$ to be significantly lower than any other wavenumbers for these parameters. With $\epsilon = 0$ and $R = 1900$, the solution drifts steadily and is dominated by the $m = 1$ wavenumber. The linear stability analysis shows that a steady flow, forced by a $Y_2^2$ heat flux heterogeneity with $\epsilon = 0.3$, is unstable to a perturbation of the $M = 1$ class (figure 9 b). A time integration of the full equations leads to a periodic solution, displayed over a full period in figure 12. The $m = 1$ and $m = 2$ flow components have the same order of magnitude of kinetic energies throughout the cycle, although the $m = 2$ energy fluctuates to a greater extent than the $m = 1$. Unlike in the periodic solution displayed in figure 10, the boundary heat-flux heterogeneity with $\epsilon = 0.3$ does not greatly inhibit the propagation of flow. Large density gradients are advected around the interior of the spherical shell by virtue of the strong $m = 1$ flow component, such that it is not even obvious that a $\cos 2\phi$ heating mode is being applied to the outer surface. This is contrast to the solution in figure 10 where the temperature maxima and minima generally occur at the outer boundary. Such large asymmetric temperature gradients could not occur in a calculation where the temperature remained fixed at the outer boundary.

The linear stability analysis shows that a substantially stronger lateral heat-flux variation of $\epsilon = 0.7$ locks the $m = 2$ symmetric thermal-wind flow with $R$ approximately 30% above $R_c$. We confirm this with time-step calculations using an ($R = 1900$,$\epsilon = 0.3$) solution as an initial condition. We now integrate the equations with $R = 2300$ and $epsilon = 0.7$, with the same initial condition. After a short transition time, the significant component in odd wavenumbers diminishes entirely and a periodic solution, containing only even wavenumbers, emerges. Like the solution in figure 10, the kinetic energy displays a large amplitude variation with time. In this case, the boundary inhomogeneity is so strong that the preference for the $m = 1$ flow favoured by the fixed-flux boundary condition plays no part in determining the symmetry of the flow.

## 7. Summary and discussion

The effect of uniform heat-flux boundary conditions on thermal instability in rotating spherical shells of radius ratio 0.4 has been investigated for infinite Prandtl number and finite Prandtl numbers between 0.1 and 10.0. The preference for large scale ($m = 1$) flows, as demonstrated by Dormy (1997), Gibbons (1998) and Takehiro *et al.* (1999), is shown to occur over a wide range of parameters (see figure 6). The effect of the thermal boundary condition (i.e. the range of Ekman numbers over which $m = 1$ is the preferred mode) is greatest for high Prandtl number and rigid fluid boundaries.

In nonlinear calculations, flows with uniform flux heating at the outer boundary display large length scale characteristics. Takehiro *et al.* (1999) performed nonlinear numerical calculations in an cylindrical annulus with inclined boundaries (see Busse 1986) and showed that, under a fixed heat-flux boundary condition, an asymmetric emergence of large and small scale cells occurs. The work presented here confirms the speculation

of Takehiro *et al.* (1999) that this effect will also arise in three-dimensional spherical geometry.

We have studied time-dependent convection subject to a lateral heat-flux variation of a $Y_2^2$ geometrical pattern for two different cases, which differ in the preferred mode of convection for the uniform heat-flux boundary problem. In the first case, the Prandtl number is low ($P_r = 0.6$) and the fixed heat-flux boundary condition is not significant in selecting the length-scale of the convective flow, $m = 2$ being optimal for heat transport. Applying a small lateral heat-flux variation drives a thermal wind flow which, as the Rayleigh number is increased, becomes unstable to perturbations of the same symmetry. For a laterally varying heat-flux of 30% of the mean radial temperature gradient, we have demonstrated a periodic flow where the $m = 2$ symmetry is not broken. Here, there are large oscillations in the kinetic energy as the large length-scale part of the flow breaks down into smaller ($m = 4$) convection cells in order to propagate past the imposed heat-flux pattern. Increasing the strength of the lateral flux variation to 40% of the vertical stabilises the thermal wind flow against perturbations with the same symmetry, and the instabilities which now arise contain components with odd-numbered $m$. The symmetry of the resulting time-dependent flow is broken and the dramatic oscillations in the kinetic energy observed previously are not exhibited.

In the second case, the higher Prandtl number ($P_r = 6.0$) means that the thermal boundary condition is more significant in selecting the mode of convection in the uniform boundary case, and the $m = 1$ mode is the most unstable. Applying a moderate lateral heat-flux variation at the surface (30% of the radial temperature gradient) results in a periodic flow where the $m = 1$ (preferred mode of convection) and $m = 2$ (imposed by boundary heating) components compete. When the lateral heat-flux variation is far stronger (70% of the radial temperature gradient), the temperature distribution which

supports the $m = 1$ flow is no longer able to exist and the resulting flow has an $m = 2$ symmetry; either boundary-locked or, at higher Rayleigh number, periodic with a similar behaviour to that observed for the lower Prandtl number.

For uniform boundary heat-flux, the large length-scale toroidal flow results from the density gradients which are able to exist near the outer boundary when the heat-flux and not the temperature is held constant. It is the action of the Coriolis force which ultimately destroys this strong horizontal flow (at low Ekman number) as the convection is forced to align with the rotation axis. It is conceivable that, in the presence of a strong magnetic field, the Lorentz force could counteract the effects of rotation sufficiently to allow such a surface flow. It is unclear how low $E$ needs to become for such thermal effects to be insignificant. However, figure (6) shows that even in the non-magnetic case, when the effects of rotation are the greatest, the large scale flows can occur for most of the parameter space over which the full dynamo problem is currently numerically tractable. An east-west hemispherical asymmetry in surface flow and secular variation is observed for an interval of time in the dynamic dynamo calculation of Kuang & Bloxham (1998). This model also has fixed heat-flux as the outer boundary condition and it may be speculated that this results from processes demonstrated here.

S.G. was supported at the University of Exeter by PPARC grant GR/L22973. The ARPACK eigenvalue software, which is incorporated into much of the code used in this study, is available from `http://www.caam.rice.edu/software/ARPACK/`

## REFERENCES

Ardes, M., Busse, F. H. & Wicht, J. 1997 Thermal convection in rotating spherical shells. *Phys. Earth Planet. Inter.* **99**, 55–67.

ARNOLDI, W. E. 1951 The principle of minimized iterations in the solution of the matrix eigenvalue problem. *Quart. J. Appl. Math.* **9**, 17–29.

BLOXHAM, J. 2000 The effect of thermal core-mantle interactions on the paleomagnetic secular variation. *Phil. Trans. R. Soc. Lond.* A**358**, 1171–1179.

BLOXHAM, J. & GUBBINS, D. 1987 Thermal core-mantle interactions. *Nature* **325**, 511–513.

BLOXHAM, J., GUBBINS, D. & JACKSON, A. 1989 Geomagnetic secular variation. *Phil. Trans. R. Soc. Lond.* A**329**, 415–502.

BUSSE, F. H. 1970 Thermal instabilities in rapidly rotating systems. *J. Fluid Mech.* **44**, 441–460.

BUSSE, F. H. 1986 Asymptotic theory of convection in a rotating, cylindrical annulus. *J. Fluid Mech.* **173**, 545–556.

CHANDRASEKHAR, S. 1961 *Hydrodynamic and hydromagnetic stability*. Clarendon.

CHRISTENSEN, U. R., AUBERT, J., CARDIN, P., DORMY, E., GIBBONS, S., GLATZMAIER, G. A., GROTE, E., HONKURA, Y., JONES, C., KONO, M., MATSUSHIMA, M., SAKURABA, A., TAKAHASHI, F., TILGNER, A., WICHT, J. & ZHANG, K. 2000 A numerical dynamo benchmark. *Phys. Earth Planet. Inter.* (submitted).

DORMY, E. 1997 Modeélisation numérique de la dynamo terrestre. PhD thesis, l'Institute de Physique du Globe de Paris.

GIBBONS, S. J. 1998 Dynamo models for the earth's magnetic field. PhD thesis, University of Leeds.

GIBBONS, S. J. & GUBBINS, D. 2000 Convection in the earth's core driven by lateral variations in the core-mantle boundary heat flux. *Geophys. J. Int.* **143**, 631–642.

GLATZMAIER, G. A. & ROBERTS, P. H. 1997 Simulating the geodynamo. *Contemporary Phys.* **38**, 269–288.

GUBBINS, D. & KELLY, P. 1993 Persistent patterns in the geomagnetic field over the past 2.5 myr. *Nature* **365**, 829–832.

GUBBINS, D. & RICHARDS, M. 1986 Coupling of the core dynamo and mantle: thermal or topographic? *Geophys. Res. Lett.* **13**, 1521–1524.

GUBBINS, D. & ZHANG, K. 1993 Symmetry properties of the dynamo equations for paleomagnetism and geomagnetism. *Phys. Earth Planet. Int.* **75**, 225–241.

HUTCHESON, K. & GUBBINS, D. 1990 A model of the geomagnetic field for the 17th century. *J. Geophys. Res.* **95**, 10769–10781.

JOHNSON, C. & CONSTABLE, C. 1995 The time-averaged geomagnetic field as recorded by lava flows over the past 5mr. *Geophys. J. Int.* **122**, 489–519.

JONES, C. A., SOWARD, A. M. & MUSSA, A. I. 2000 The onset of thermal convection in a rapidly rotating sphere. *J. Fluid Mech.* **405**, 157–179.

KARATO, S. 1993 Importance of anelasticity in the interpretation of seismic tomography. *Geophys. Res. Lett.* **20**, 1623–1626.

KUANG, W. & BLOXHAM, J. 1998 Numerical dynamo modelling: Comparison with the earth's magnetic field. In *The Core-Mantle Boundary Region* (ed. M. Gurnis, M. E. Wysession, E. Knittle & B. A. Buffett), pp. 197–208. American Geophysical Union.

LEHOUCQ, R. B., SORENSEN, D. C. & YANG, C. 1998 *Arpack users guide: Solution of large scale eigenvalue problems by implicitly restarted Arnoldi methods*. SIAM.

MASTERS, G., JOHNSON, S., LASKE, G. & BOLTON, H. 1996 A shear-velocity model of the mantle. *Phil. Trans. R. Soc. Lond.* A**354**, 1385–1411.

MASTERS, T. G. & SHEARER, P. M. 1995 Seismic models of the earth: Elastic and anelastic. In *Global Earth Physics* (ed. T. J. Ahrens), pp. 88–103. American Geophysical Union.

OLSON, P. & GLATZMAIER, G. 1996 Magnetoconvection and thermal coupling of the earth's core and mantle. *Phil. Trans. R. Soc. Lond.* A**354**, 1413–1424.

ROBERTS, P. H. 1968 On the thermal instability of a rotating fluid sphere containing heat sources. *Phil. Trans. R. Soc. Lond.* A**263**, 93–117.

SARSON, G. R., JONES, C. A. & LONGBOTTOM, A. W. 1997 The influence of boundary region heterogeneities on the geodynamo. *Phys. Earth planet. Inter.* **101**, 13–32.

SORENSEN, D. C. 1992 Implicit application of polynomial filters in a $k$-step Arnoldi method. *SIAM J. Matrix Analysis and Applications* **13**, 357–385.

STACEY, F. D. 1995 Theory of thermal and elastic properties of the lower mantle and core. *Phys. Earth Planet. Inter.* **89**, 219–245.

STACEY, F. D. 1998 Thermoelasticity of a mineral composite and a reconsideration of lower mantle properties. *Phys. Earth Planet. Inter.* **106**, 219–236.

SU, W. & DZIEWONSKI, A. M. 1991 Predominance of long-wavelength heterogeneity in the mantle. *Nature* **352**, 121–126.

SUN, Z. P., SCHUBERT, G. & GLATZMAIER, G. A. 1993 Transitions to chaotic thermal convection in a rapidly rotating spherical fluid shell. *Geophys. Astrophys. Fluid Dyn.* **69**, 95–131.

SUN, Z. P., SCHUBERT, G. & GLATZMAIER, G. A. 1994 Numerical simulations of thermal convection in a rapidly rotating spherical shell cooled inhomogeneously from above. *Geophys. Astrophys. Fluid Dyn.* **75**, 199–226.

TAKEHIRO, S., ISHIWATARI, M., NAKAJIMA, K. & HAYASHI, Y. Y. 1999 The effects of thermal boundary condition on convection in rapidly rotating spherical shells. In *Theoretical and applied mechanics: proceedings of the 48th Japan National Congress for Applied Mechanics, 1999* (ed. Y. Miyake), pp. 415–421. University of Tokyo Press.

TILGNER, A. & BUSSE, F. H. 1997 Finite-amplitude convection in rotating spherical fluid shells. *J. Fluid Mech.* **332**, 359–376.

YANO, J. I. 1992 Asymptotic theory of thermal convection in rapidly rotating systems. *J. Fluid Mech.* **243**, 103–131.

ZHANG, K. 1991 Convection in a rapidly rotating spherical shell at infinite Prandtl number: steadily drifting rolls. *Phys. Earth Planet. Inter.* **68**, 156–169.

ZHANG, K. 1992 Spiralling columnar convection in rapidly rotating spherical fluid shells. *J. Fluid Mech.* **236**, 535–556.

ZHANG, K. & BUSSE, F. H. 1987 On the onset of convection in rotating spherical shells. *Geophys. Astrophys. Fluid Dyn.* **39**, 119–147.

ZHANG, K. & GUBBINS, D. 1992 On convection in the earth's core driven by lateral temperature variations in the lower mantle. *Geophys. J. Int.* **102**, 247–255.

ZHANG, K. & GUBBINS, D. 1993 Convection in a rotating spherical fluid shell with an inhomogeneous temperature boundary condition at infinite Prandtl number. *J. Fluid Mech.* **250**, 209–232.

ZHANG, K. & GUBBINS, D. 1996 Convection in a rotating spherical fluid shell with an inhomogeneous temperature boundary condition at finite Prandtl number. *Phys. Fluids* **8**, 1141–1148.

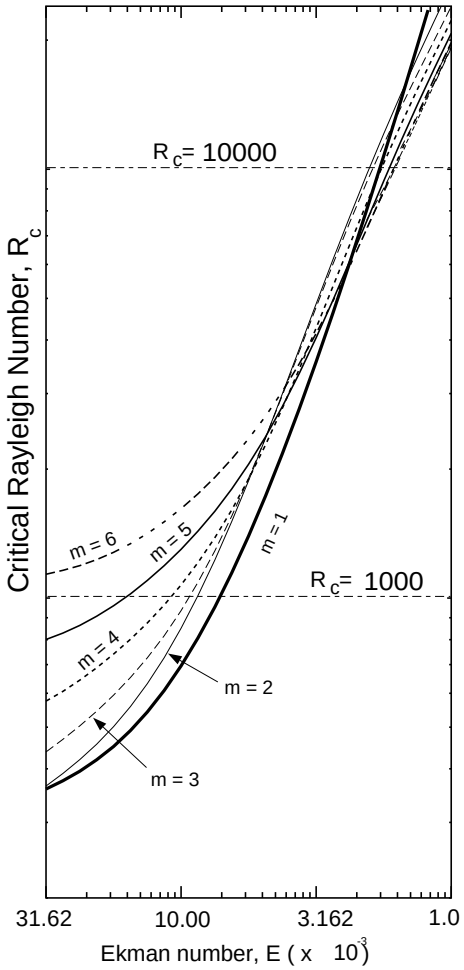


FIGURE 1. Critical Rayleigh number, $R_c$, as a function of the Ekman number, $E$, for $m = 1$ to $m = 6$ in the range $3.162 \times 10^{-2} \geq E \geq 10^{-3}$ with infinite Prandtl number, $\eta = 0.4$ and stress-free boundaries. Heat flux is kept uniform at outer boundary. Both axes are scaled logarithmically.

ZHANG, K. & JONES, C. A. 1993 The influence of Ekman boundary layers on rotating convection. *Geophys. Astrophys. Fluid Dyn.* **71**, 145–162.

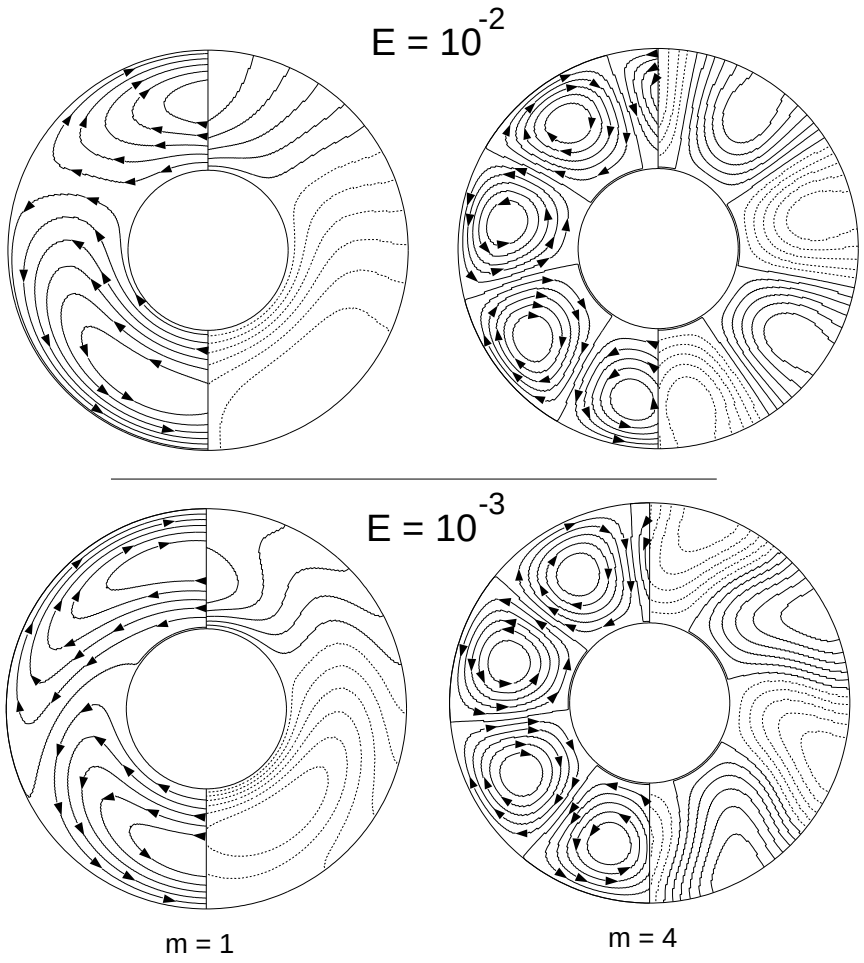


FIGURE 2. $m = 1$ and $m = 4$ solutions in the equatorial plane of a drifting frame of reference for $\eta = 0.4$, infinite Prandtl number, stress-free boundaries and uniform heat flux at the outer boundary. Values of $E$ are as shown; left sides of plots are streamlines of flow with $0 \leq \phi \leq \pi$ and right sides of plots are contours of temperature variations with $\pi \leq \phi \leq 2\pi$. Contours are evenly spaced and vary between plots. Dotted lines indicate negative values. $R_c(m = 1) = 695.3$ and $R_c(m = 4) = 1073.4$ at $E = 10^{-2}$. $R_c(m = 1) = 32776$ and $R_c(m = 4) = 19737$ at $E = 10^{-3}$.

| Truncation ($L/N$) | $m$ | Critical Rayleigh number, $R_c$ (osc. freq., $\sigma_{\rm i}$) | |
|---|---|---|---|
| | | ($E = 1.4035 \times 10^{-4}$) | ($E = 1.3947 \times 10^{-4}$) |
| (26/50) | 1 | 161141.5 (8.3337) | 163493.1 (8.4254) |
| (28/100) | 1 | 160401.4 (8.2891) | 162731.4 (8.3796) |
| (28/150) | 1 | 160350.5 (8.2859) | 162677.7 (8.3762) |
| (30/150) | 1 | 160330.0 (8.2847) | 162657.0 (8.3750) |
| (32/150) | 1 | 160323.4 (8.2843) | 162650.8 (8.3746) |
| (28/150) | 10 | 162096.4 (83.497) | 163516.7 (84.009) |
| (32/150) | 10 | 161979.5 (83.482) | 163394.8 (83.992) |
| (26/50) | 11 | 161334.9 (80.902) | 162724.4 (81.430) |
| (28/100) | 11 | 161142.3 (80.732) | 162529.2 (81.259) |
| (28/150) | 11 | 161129.1 (80.720) | 162515.8 (81.247) |
| (30/150) | 11 | 161136.3 (80.719) | 162523.3 (81.246) |
| (32/150) | 11 | 161140.1 (80.720) | 162527.2 (81.246) |
| (28/150) | 12 | 161339.4 (77.210) | 162707.8 (77.748) |
| (32/150) | 12 | 161316.6 (77.211) | 162684.0 (77.749) |
| (32/150) | 13 | 162272.7 (73.038) | 163624.9 (73.585) |

TABLE 1. Critical Rayleigh numbers, $R_c$, for selected wavenumbers, infinite $P_r$, fixed heat flux at $r = r_{\rm o}$, rigid velocity boundaries and the Ekman numbers $E = 1.4035 \times 10^{-4}$ and $E = 1.3947 \times 10^{-4}$. $R_c$ is higher than those shown for all other wavenumbers. The oscillation frequency, $\sigma_{\rm i}$, is given in brackets.

| $E$ | $R_c$ $(m = 7)$ | $R_c$ $(m = 8)$ |
|---|---|---|
| $1.8900 \times 10^{-3}$ | 9933 | 10049 |
| $1.4142 \times 10^{-3}$ | 14193 | 14107 |
| $8.1650 \times 10^{-4}$ | 26660 | 26843 |

TABLE 2. Critical Rayleigh numbers, $R_c$, for $m = 7$ and $m = 8$ for infinite $P_r$, fixed heat flux at $r = r_o$ and stress-free boundaries. For these parameters, $R_c$ for all other wavenumbers is higher than those for $m = 7$ and $m = 8$. Figures are converged to 0.02%.

| $m$ | $R_c$ with $P_r = 0.6$ | $R_c$ with $P_r = 6.0$ |
|---|---|---|
| 1 | 1145.1 | 1588.5 |
| 2 | 1053.1 | 2027.0 |
| 3 | 1104.2 | 2050.5 |
| 4 | 1350.5 | 2059.5 |
| 5 | 1801.6 | 2241.4 |
| 6 | 2410.8 | 2572.8 |

TABLE 3. Critical Rayleigh numbers, $R_c$, for selected wavenumbers, with uniform heat flux at $r = r_o$, stress-free velocity boundaries and the $E = 5 \times 10^{-3}$. Figures are converged to 0.01%.

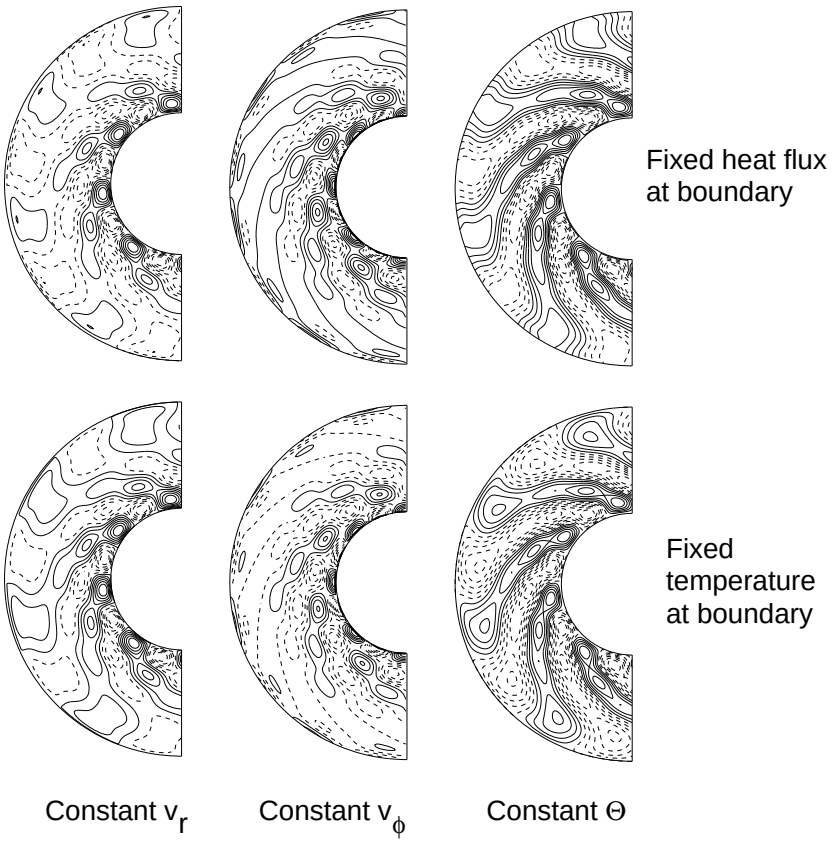


FIGURE 3. Solutions at $E = 3.162 \times 10^{-4}$ for the $m = 8$ modes for both fixed temperature and fixed heat-flux outer boundary conditions. Solutions are shown at onset in the equatorial plane ($\theta = \pi/2, 0 \leq \phi \leq \pi$) in a rotating frame of reference. Contour levels vary between plots. Boundaries are stress-free and $P_r$ is infinite.

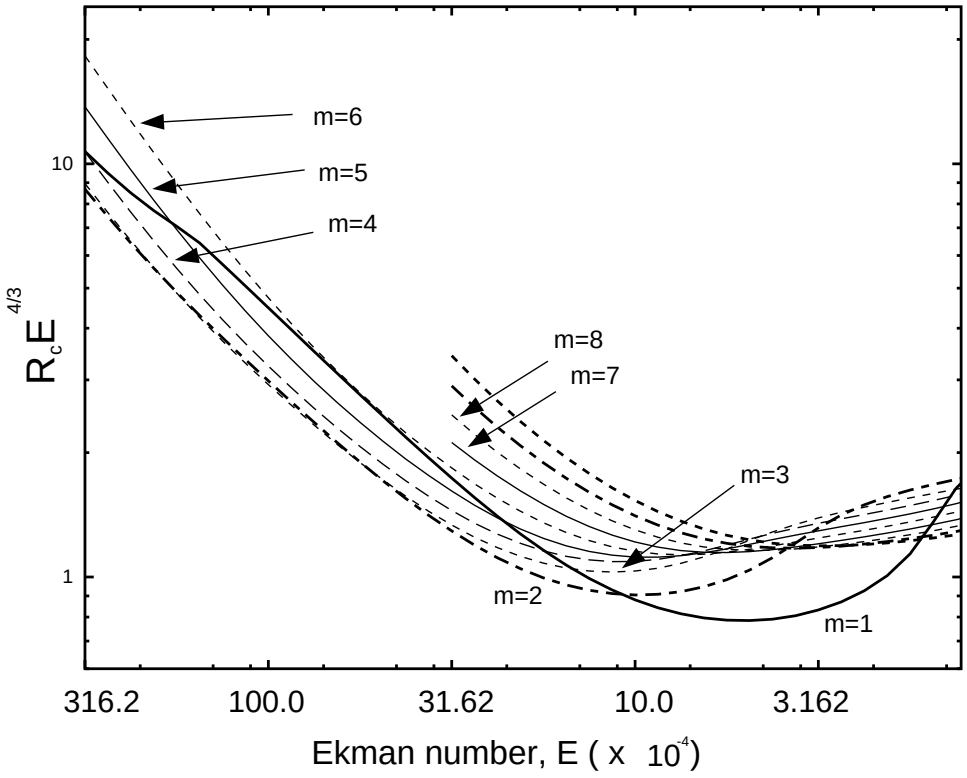


FIGURE 4. $R_cE^{4/3}$, as a function of the Ekman number, $E$, for $m = 1$ to $m = 10$ in the range $3.162 \times 10^{-2} \geq E \geq 10^{-4}$ with infinite Prandtl number, $\eta = 0.4$ and rigid boundaries. Heat flux kept uniform at outer boundary.

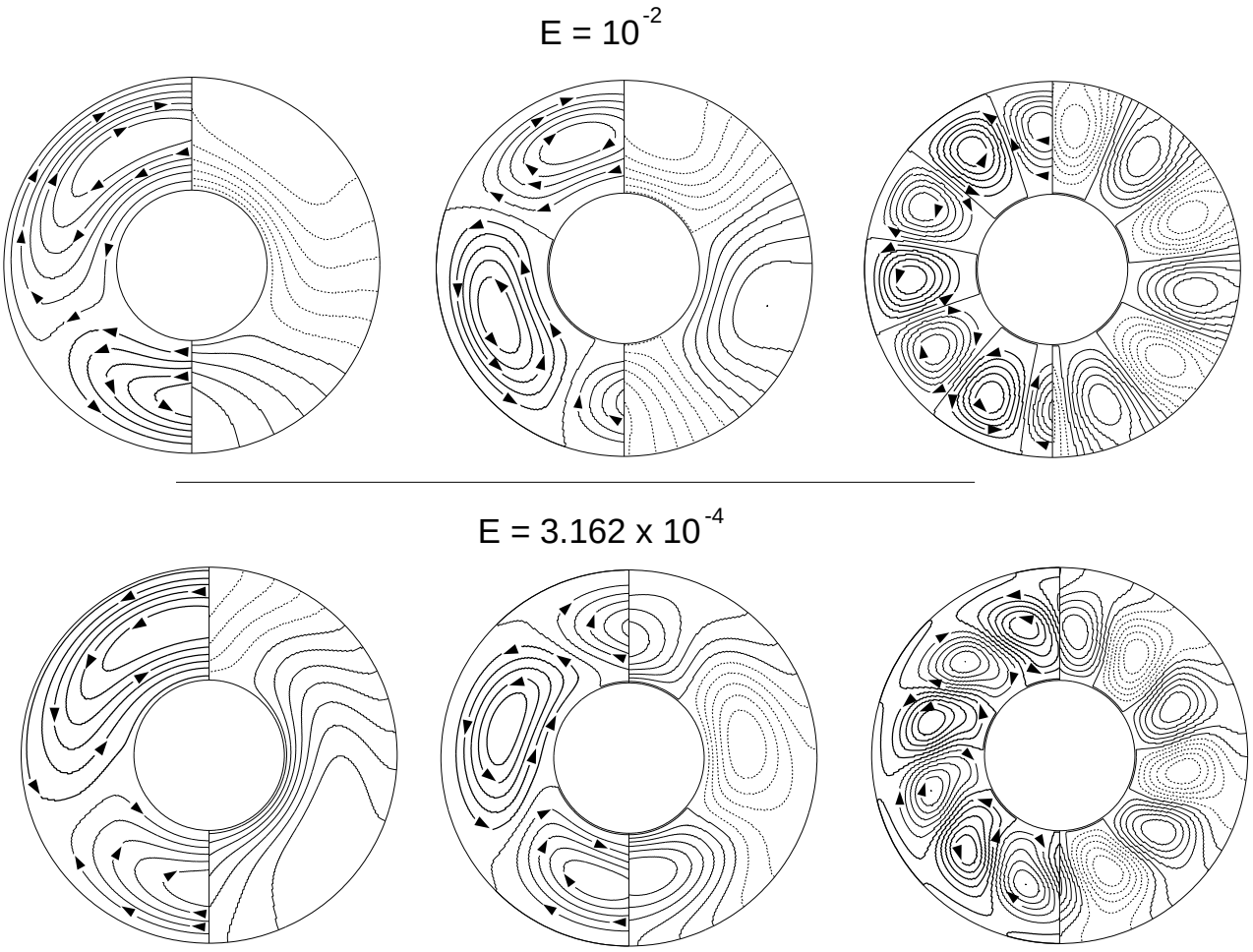


FIGURE 5. Solutions for $m = 1$, $m = 2$ and $m = 6$ modes at $E = 10^{-2}$ and $E = 3.162 \times 10^{-4}$ when $\eta = 0.4$, heat flux is kept constant at the outer surface and boundaries are rigid. All plots show, in a rotating frame of reference, lines of flow in the equatorial section $\theta = \pi/2$ , $0 \leq \phi \leq \pi$ (left side diagrams) and contours of $\Theta$ in the equatorial section $\theta = \pi/2$ , $\pi \leq \phi \leq 2\pi$ (right side diagrams). In the case $E = 10^{-2}$; $R_c(m = 1) = 20804$, $R_c(m = 2) = 13848$ and $R_c(m = 6) = 22004$. In the case $E = 3.162 \times 10^{-4}$; $R_c(m = 1) = 38717$, $R_c(m = 2) = 59542$ and $R_c(m = 6) = 56257$.

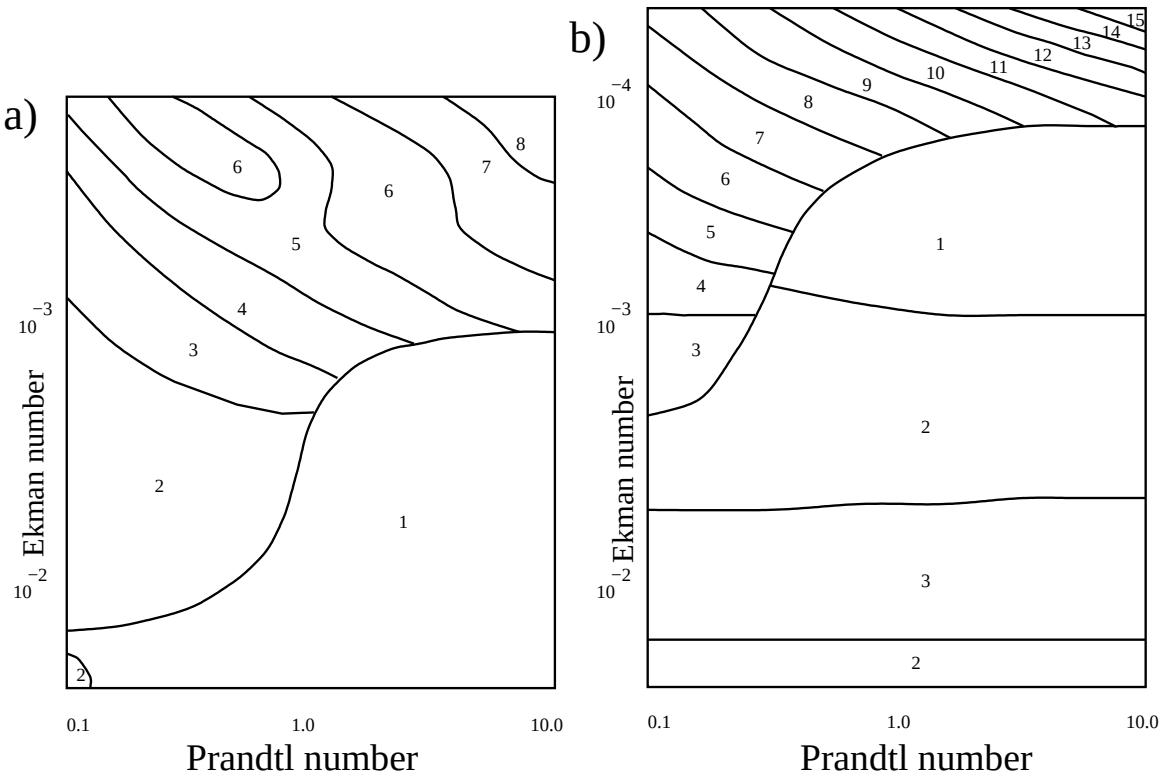


FIGURE 6. Critical mode, $m_c$, as a function of $E$ and $P_r$ for the case of a) stress-free boundaries and b) rigid boundaries. Both axes have logarithmic scaling.

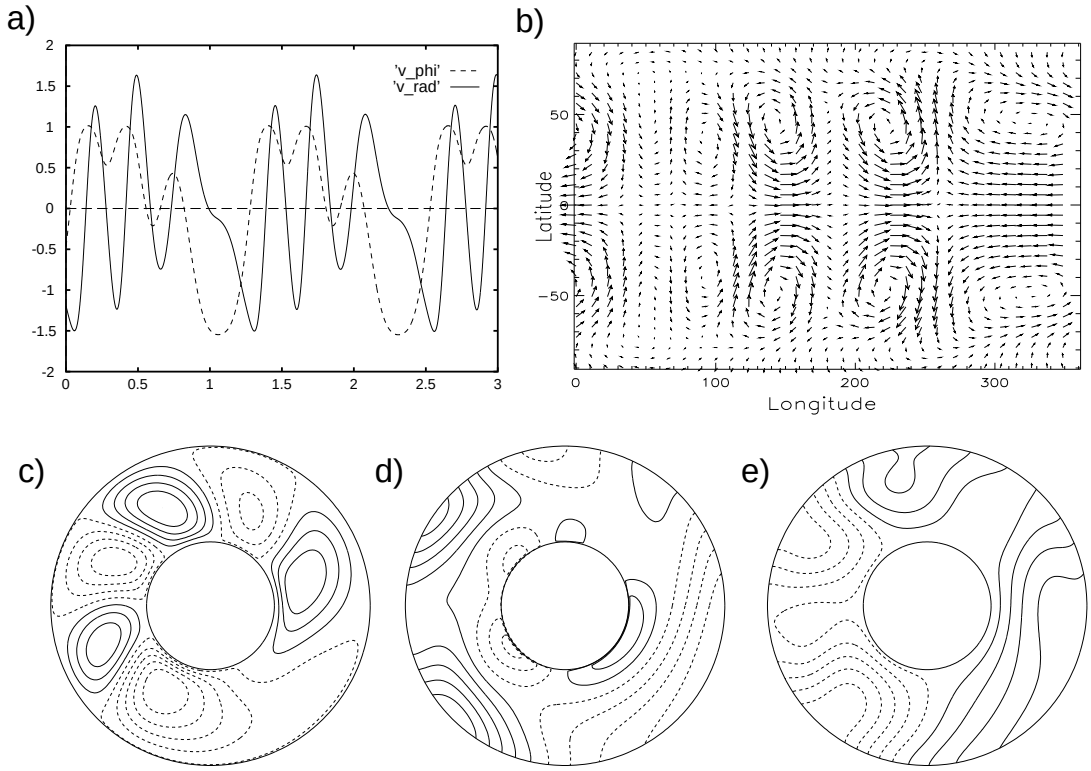


FIGURE 7. Finite amplitude convection solution for $E = 2.8 \times 10^{-3}$, $P_r = 10$, $R = 4900$ with uniform heat-flux at the outer boundary and stress-free boundaries. a) Shows $v_\phi$ and $v_r$ evaluated at $\phi = 0$, $\theta = \pi/2$ and $r = (r_\mathrm{i} + r_\mathrm{o})/2$ as a function of time. b) shows arrows indicating relative strength and direction of flow just below the outer surface. c), d) and e) respectively show contours of $v_r$, $v_\phi$ and $\Theta$ in the equatorial plane. Solid contours represent positive values and dashed contours represent negative values.

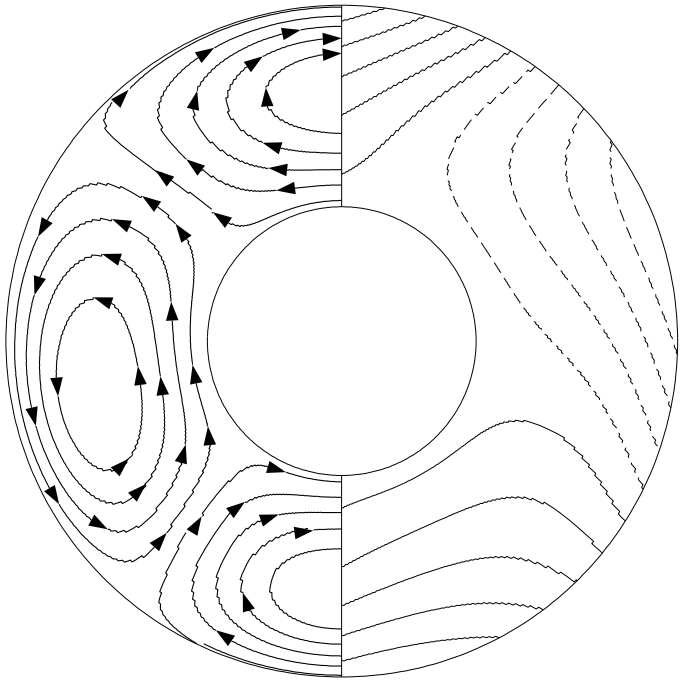

FIGURE 8. Lines of flow (left) and contours of temperature (right) in equatorial section for the steady flow locked by a $Y_2^{2c}$ variation in the heat-flux at the outer boundary. $R = 800$, $\epsilon = 0.3$, $P_r = 0.6$, $E = 5 \times 10^{-3}$, and boundaries are stress-free.

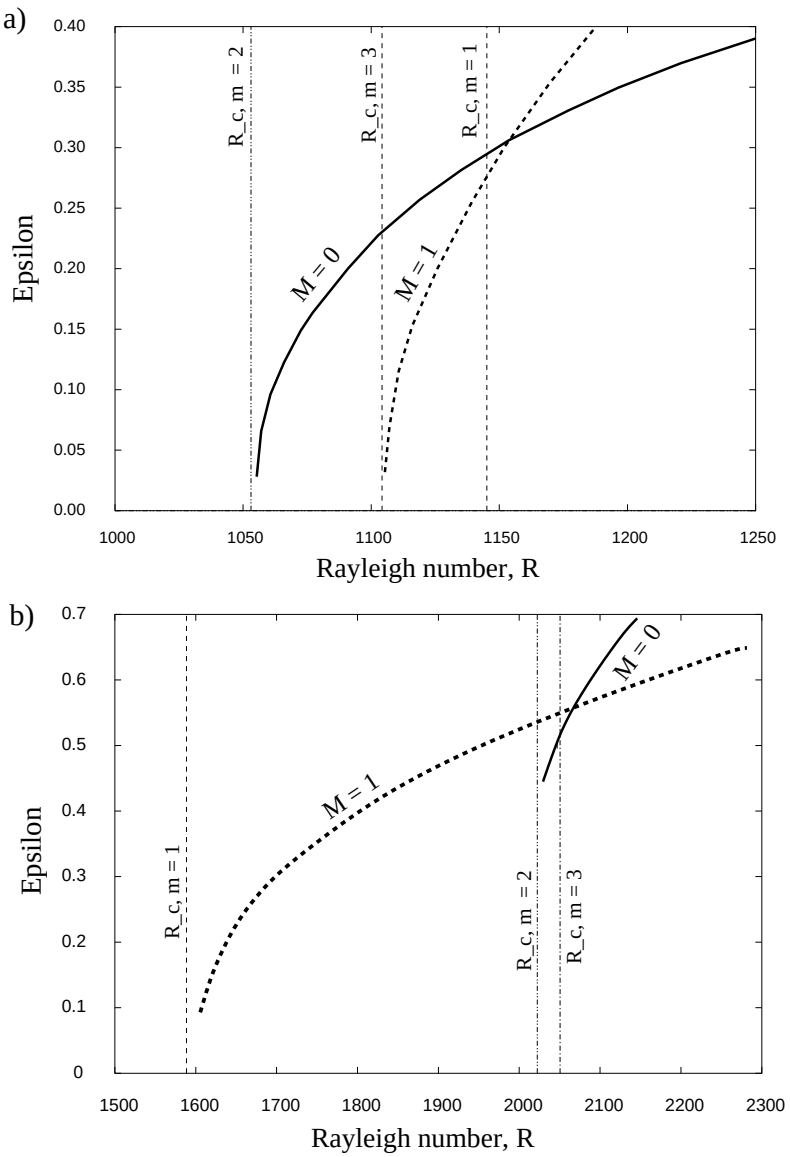


FIGURE 9. Lines of critical stability $R_s(0)$ and $R_s(1)$ for perturbations to steady flows locked by a $Y_2^{2c}$ variation in the heat-flux at the outer boundary. $R_c$ denotes the critical Rayleigh number for the onset of thermal instability with $\epsilon = 0$. $P_r = 0.6$(a) and 6.0(b), $E = 5 \times 10^{-3}$ and boundaries are stress-free.

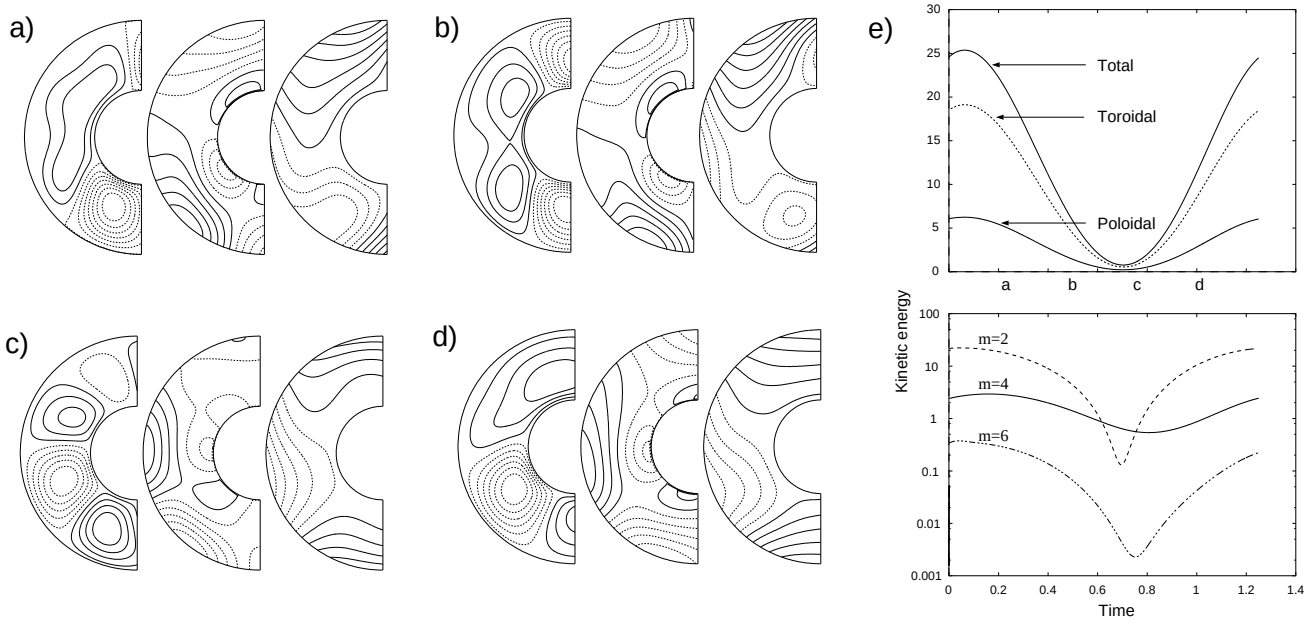


FIGURE 10. Periodic solution for $E = 5 \times 10^{-3}$, $R = 1200$, $\epsilon = 0.30$, $P_r = 0.6$ and $g = Y_2^{2c}$. Diagram e) shows the kinetic energy in various velocity components against time. The plots show contours of $v_r$ (left), $v_\phi$ (centre) and $T$ (right) in an equatorial half plane for the times $t = 0.25$ (a), $t = 0.50$ (b), $t = 0.75$ (c) and $t = 1.00$ (d).

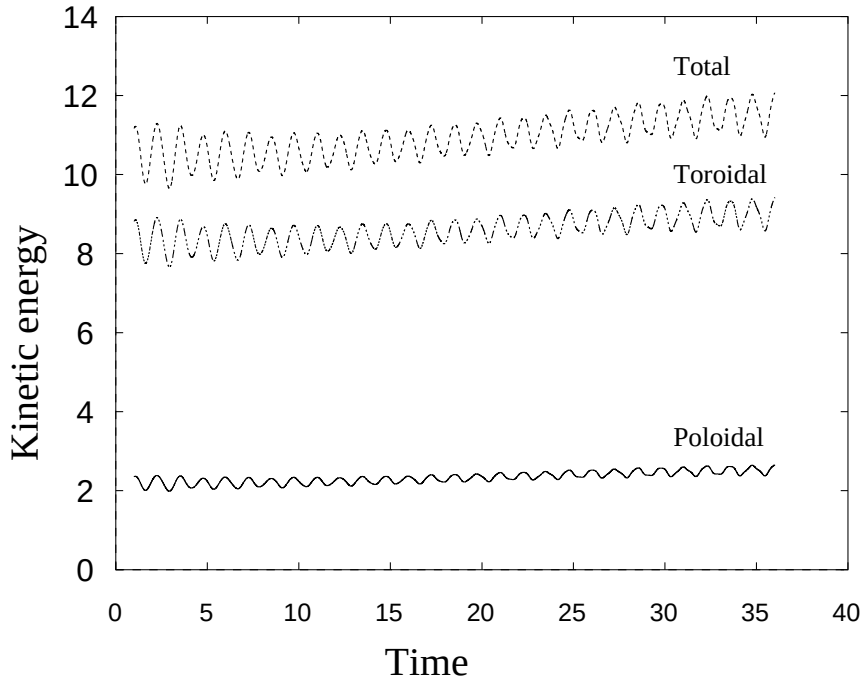


FIGURE 11. Kinetic energy of flow subject to a $Y_2^{2c}$ heat-flux variation for $R = 1200$, $\epsilon = 0.4$, $P_r = 0.6$, $E = 5 \times 10^{-3}$ and stress-free boundaries.

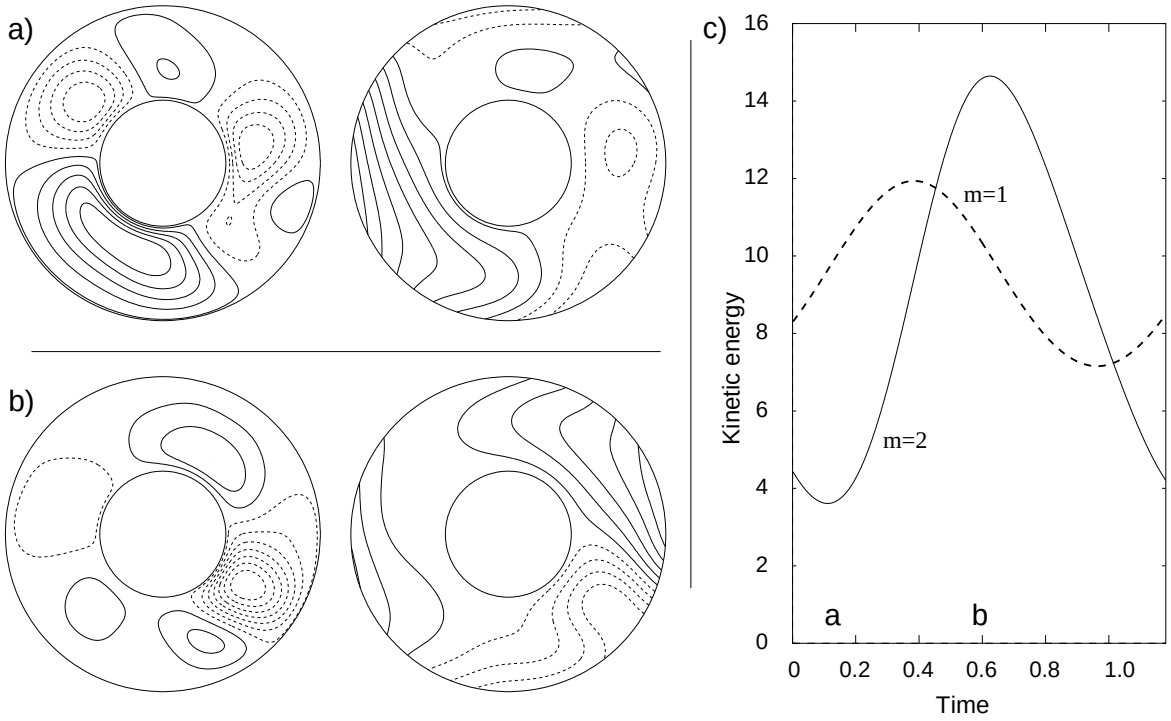


FIGURE 12. Periodic solution for $E = 5 \times 10^{-3}$, $R = 1900$, $\epsilon = 0.30$, $P_r = 6.0$ and $g = Y_2^{2c}$. Diagram c) shows the kinetic energy in the velocity components with $m = 1$ and $m = 2$ (the energy in other wavenumbers is insignificant). The plots show contours of $v_r$ (left) and $T$ (right) in an equatorial section for the times $t = 0.125$ (a) and $t = 0.625$ (b).